Oceanic mesoscale eddy depletion catalyzed by internal waves

Roy Barkan[1], Kaushik Srinivasan[2], Luwei Yang[3], James C. McWilliams[2], Jonathan Gula[4], and Clément Vic[5]

[1]Tel Aviv University
[2]University of California Los Angeles
[3]UCLA
[4]Université de Bretagne Occidentale
[5]University of Southampton

November 24, 2022

Abstract

The processes leading to the depletion of oceanic mesoscale kinetic energy (KE) and the energization of near-inertial internal waves are investigated using a suite of realistically forced regional ocean simulations. By carefully modifying the forcing fields we show that solutions where internal waves are forced have ˜25% less mesoscale KE compared with solutions where they are not. We apply a coarse-graining method to quantify the KE fluxes across time scales and demonstrate that the decrease in mesoscale KE is a result of an internal wave-induced reduction of the inverse energy cascade and an enhancement of the forward energy cascade from sub- to super-inertial frequencies. The integrated KE forward transfer rate in the upper ocean is equivalent to half and a quarter of the regionally averaged near-inertial wind work in winter and summer, respectively, with the strongest fluxes localized at surface submesoscale fronts and filaments.

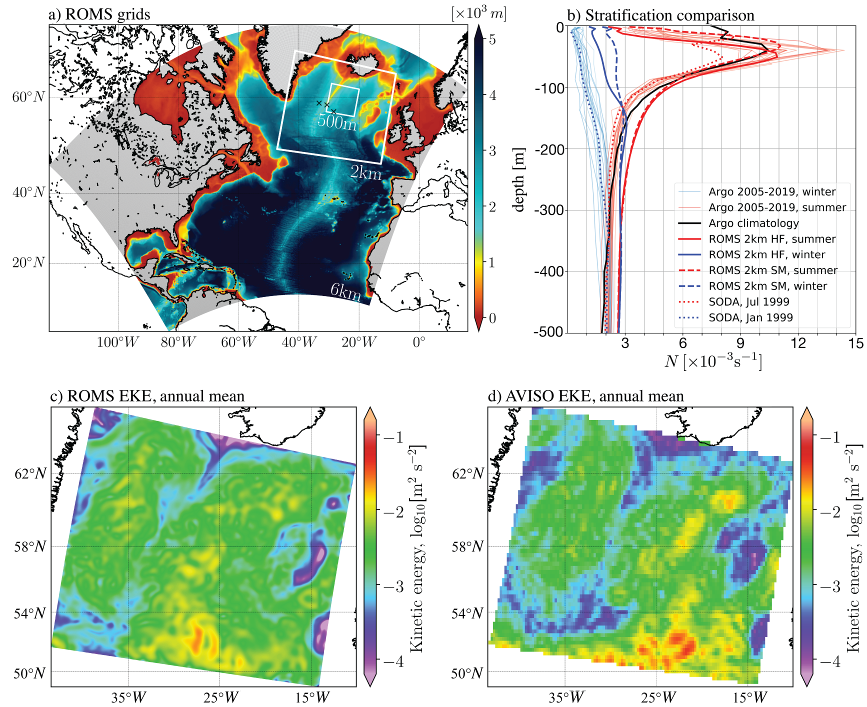
a) ROMS grids
[×10^3 m]
500m
2km
6km
60°N
40°N
20°N
100°W
80°W
60°W
40°W
20°W
0°
b) Stratification comparison
depth [m]
Argo 2005-2019, winter
Argo 2005-2019, summer
Argo climatology
ROMS 2km HF, summer
ROMS 2km HF, winter
ROMS 2km SM, summer
ROMS 2km SM, winter
SODA, Jul 1999
SODA, Jan 1999
N [×10^-3 s^-1]
c) ROMS EKE, annual mean
d) AVISO EKE, annual mean
Kinetic energy, log10[m^2 s^-2]
62°N
58°N
54°N
50°N
35°W
25°W
15°W

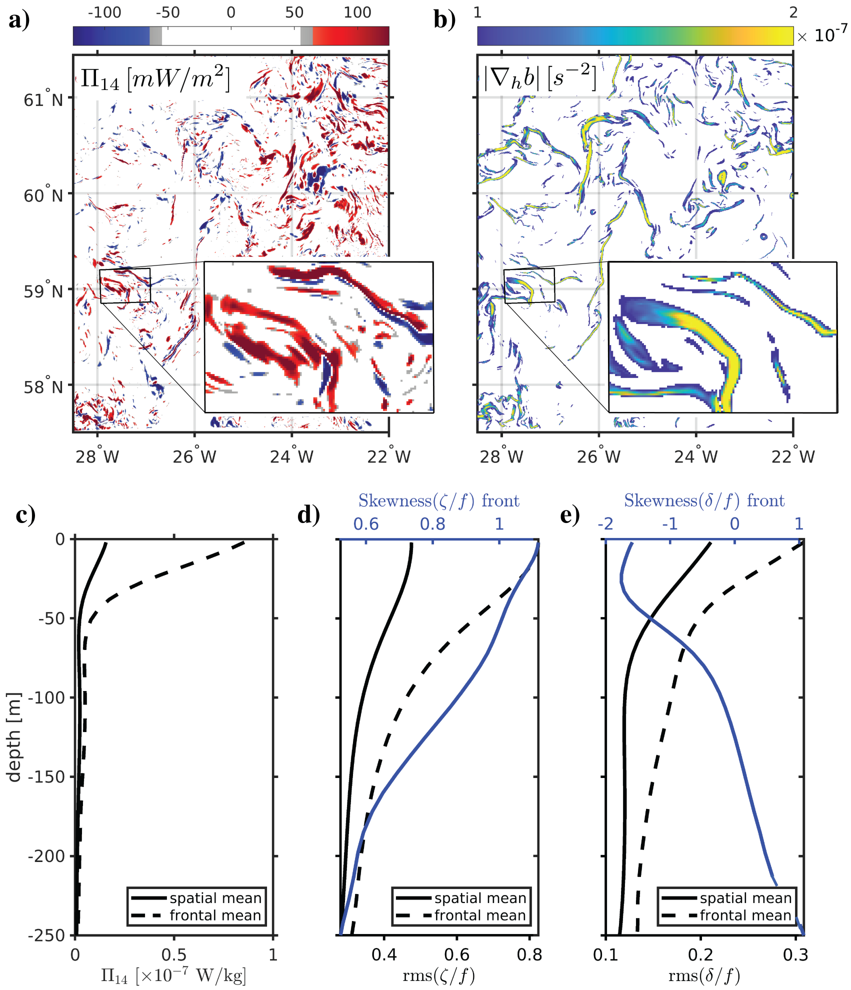
a)
b)
$\Pi_{14}\ [mW/m^2]$
$|\nabla_h b|\ [s^{-2}]$
-100 -50 0 50 100
1 2 $\times 10^{-7}$
61°N
60°N
59°N
58°N
28°W 26°W 24°W 22°W
c)
d)
e)
depth [m]
0 -50 -100 -150 -200 -250
Π_{14} [$\times 10^{-7}$ W/kg]
0 0.5 1
Skewness(ζ/f) front
0.6 0.8 1
rms(ζ/f)
0.4 0.6 0.8
Skewness(δ/f) front
-2 -1 0 1
rms(δ/f)
0.1 0.2 0.3
spatial mean
frontal mean

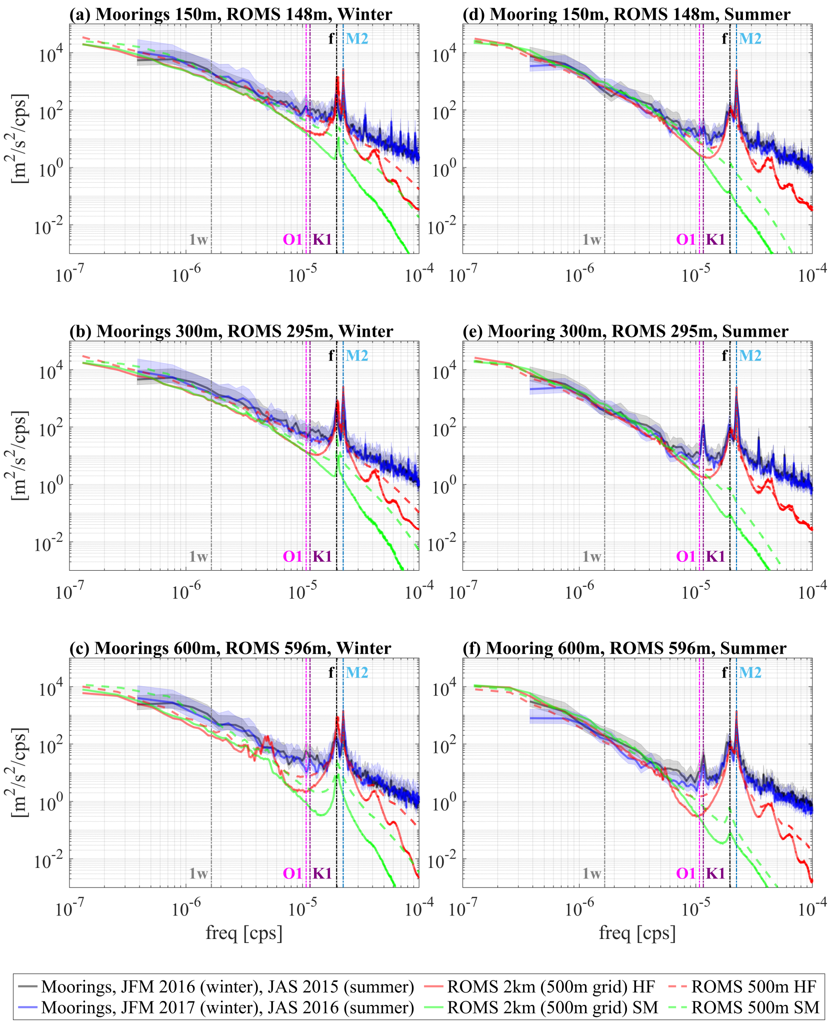

(a) Moorings 150m, ROMS 148m, Winter
(d) Mooring 150m, ROMS 148m, Summer
(b) Moorings 300m, ROMS 295m, Winter
(e) Mooring 300m, ROMS 295m, Summer
(c) Moorings 600m, ROMS 596m, Winter
(f) Mooring 600m, ROMS 596m, Summer
[m²/s²/cps]
freq [cps]
1w
O1
K1
f
M2
Moorings, JFM 2016 (winter), JAS 2015 (summer)
Moorings, JFM 2017 (winter), JAS 2016 (summer)
ROMS 2km (500m grid) HF
ROMS 2km (500m grid) SM
ROMS 500m HF
ROMS 500m SM

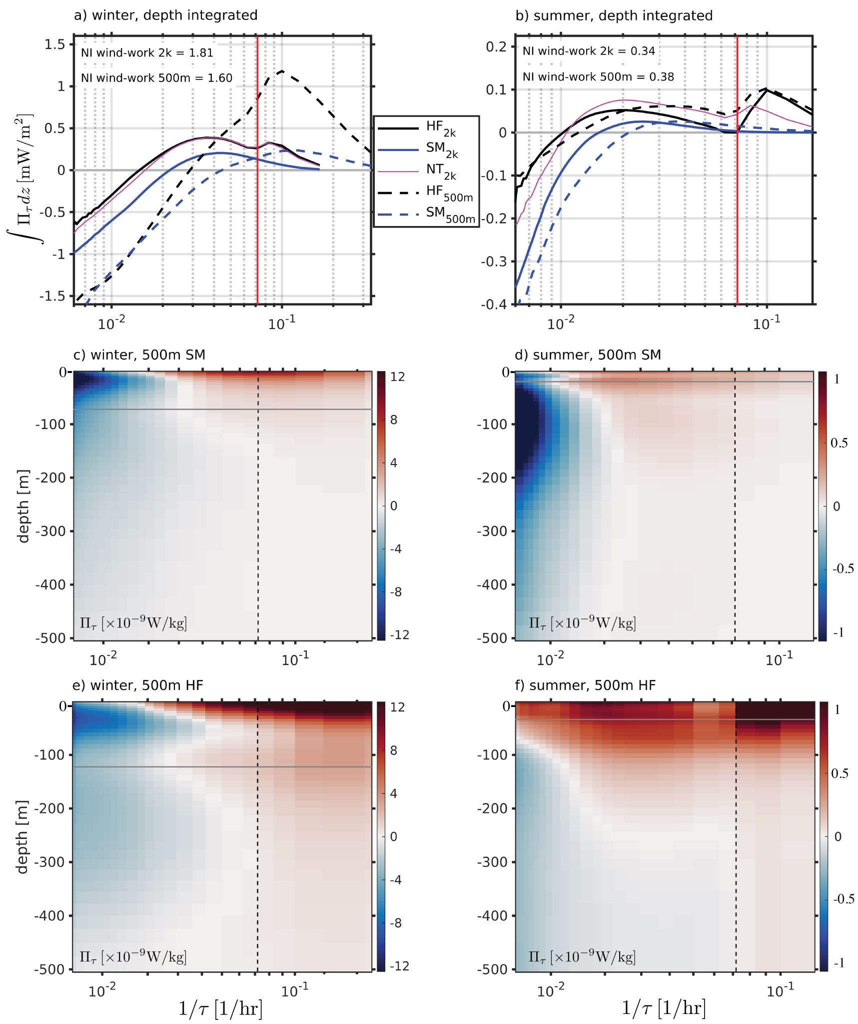

a) winter, depth integrated
b) summer, depth integrated
NI wind-work 2k = 1.81
NI wind-work 500m = 1.60
NI wind-work 2k = 0.34
NI wind-work 500m = 0.38
HF2k
SM2k
NT2k
HF500m
SM500m
c) winter, 500m SM
d) summer, 500m SM
e) winter, 500m HF
f) summer, 500m HF
depth [m]
1/τ [1/hr]

Oceanic mesoscale eddy depletion catalyzed by internal waves

Roy Barkan[1,2], Kaushik Srinivasan[2], Luwei Yang[2], James C. McWilliams[2], Jonathan Gula[3,4], Clément Vic[3]

[1]Porter School of the Environment and Earth Sciences, Tel Aviv University, Ramat Aviv, Israel 6997801
[2]Department of Atmospheric and Oceanic Sciences, University of California, Los Angeles, CA 90095
[3]Laboratoire d'Océanographie Physique et Spatiale, Université de Bretagne Occidentale, Plouzané, France 29280
[4]Institut Universitaire de France (IUF)

Key Points:

- Wind forced near-inertial waves and internal tides can efficiently drain oceanic mesoscale eddy energy.
- Eddy energy 'draining' is largely a result of an internal-wave induced modifications to the turbulent energy cascades.
- The strongest forward energy transfers are found in submesoscale fronts and filaments that dynamically depart from geostrophic balance.

Corresponding author: Roy Barkan, `rbarkan@tauex.tau.ac.il`

Abstract

The processes leading to the depletion of oceanic mesoscale kinetic energy (KE) and the energization of near-inertial internal waves are investigated using a suite of realistically forced regional ocean simulations. By carefully modifying the forcing fields we show that solutions where internal waves are forced have $\sim 25\%$ less mesoscale KE compared with solutions where they are not. We apply a coarse-graining method to quantify the KE fluxes across time scales and demonstrate that the decrease in mesoscale KE is a result of an internal wave-induced reduction of the inverse energy cascade and an enhancement of the forward energy cascade from sub- to super-inertial frequencies. The integrated KE forward transfer rate in the upper ocean is equivalent to half and a quarter of the regionally averaged near-inertial wind work in winter and summer, respectively, with the strongest fluxes localized at surface submesoscale fronts and filaments.

Plain Language Summary

Oceanic mesoscale eddies contain most of the kinetic energy in the ocean and therefore play an important role in determining the ocean's response to future climate scenarios. Oceanic wind- and tidally-forced internal waves are energetic fast motions that contribute substantially to the vertical mixing of water, thereby affecting biogeochemical and climate processes. This work shows for the first time in high-resolution, realistically forced, numerical simulations that wave motions can drain a substantial amount of eddy energy by altering the way in which energy is transferred across scales. This has important implications to ocean energetics and to climate models that often lack the resolution and forcing components to represent these wave-induced effects.

1 Introduction

The general circulation of the ocean is strongly constrained by the pathways that kinetic and available potential energy take from the basin-scale forces that inject them to centimeter scales, where they are depleted. To determine the ocean's response to future climate scenarios, these energetic pathways, from forcing to dissipation, must be understood and quantified.

Mesoscale eddies, with horizontal scales on the order of 100 km and timescales longer than many days, are well known as the dominant reservoir of kinetic energy (KE) in the oceans (Wunsch & Ferrari, 2004). But because their dynamics are constrained by an approximate geostrophic and hydrostatic force balance, they are characterized by an inverse KE cascade, and by themselves do not provide the necessary forward scale-transfer to dissipation (Müller et al., 2005). Possible mechanisms to interrupt the mesoscale inverse cascade include interaction with the bottom topography and boundary layer (Sen et al., 2008; Arbic et al., 2009; Nikurashin et al., 2013; Trossman et al., 2013, 2016) and instabilities that are strongly linked to the formation of the more rapidly evolving submesoscale currents, with horizontal scales of about 0.1-10 km (Capet et al., 2008a; McWilliams, 2016).

Near-inertial waves (NIWs) are predominately storm-forced internal waves with an intrinsic frequency close to the local Coriolis frequency at their generation site and with horizontal scales that are initially as large as the storms that excited them (Alford et al., 2016). Mooring observations indicate that they are a significant mode of high-frequency variability in the ocean (Wunsch & Ferrari, 2004) with a comparable power input on the global scale as internal tides (G. Egbert & Ray, 2000; Alford, 2003). They are characterized by strong vertical shear (Pinkel, 2014; Alford et al., 2017) and are therefore expected to contribute to upper-ocean mixing, thereby affecting a variety of processes like biogeochemistry and climate (Jochum et al., 2013). Observational estimates of the windwork that excites NIWs depend on the estimating method and resolution of the wind product, and have global values ranging between 0.3-1.3 TW (Jiang et al., 2005; Alford, 2020). This uncertainty emphasizes the difficulty in quantifying NIW energetics in measurements.

In recent years, a growing number of theories and idealized numerical simulations of varying complexity have demonstrated that geostrophic mesoscale eddies and NIWs can interact and exchange energy (Bühler & McIntyre, 2005; Polzin, 2010; Whitt & Thomas, 2015; Xie & Vanneste, 2015; Wagner & Young, 2016; Taylor & Straub, 2016; Barkan et al., 2017; L. N. Thomas, 2017; Rocha et al., 2018; J. Thomas & Daniel, 2020). These interactions, which are hypothesized to have important implications to both mesoscale KE dissipation routes and to NIW energetics, are however poorly constrained in realistic settings.

Here, we attempt for the first time to quantify NIW-eddy interactions in a series of realistically forced numerical simulations that are validated against mooring-, satellite-, and Argo-based measurements. By comparing numerical simulations with and without externally forced NIWs and internal tides we show that solutions with internal wave (IW) forcing have roughly 25% less mesoscale KE than solutions without IW forcing during both winter and summer months. This decrease in mesoscale KE is explained by an IW-induced reduction in the inverse KE cascade to sub-inertial frequencies and an increase in the forward cascade to super-inertial frequencies — *stimulated* cascades. The strongest forward KE transfer rate is shown to be most prominent in the mixed layer during winter, to be spatially localized in regions of strong submesoscale fronts and filaments that dynamically depart from geostrophic balance, and to have magnitudes comparable to the averaged near-inertial wind work in the study region.

2 Modeling and validation

Numerical simulations were carried out using the Regional Oceanic Modeling System (ROMS; Shchepetkin & McWilliams, 2005) forced by the Climate Forecast System Reanalysis (CFSR) atmospheric product (Dee et al., 2014), with gradual nesting to zoom in on the Iceland Basin (Fig. 1a; SI-Modeling). This region has complex current-topography interactions (Fratantoni, 2001), a rich mesoscale eddy field (Jakobsen et al., 2003), strong NIW activity (Chaigneau et al., 2008), and is the target location for the Near-Inertial Shear and Kinetic Energy in the North Atlantic experiment (L. N. Thomas et al., 2020).

The presented analysis is based on three simulation sets with 2 km and 500 m horizontal grid spacing. The first set (high-frequency forcing; herein after HF) is forced by hourly winds, hourly boundary conditions from the parent 6 km solution, and includes TPXO-based (G. D. Egbert et al., 1994; G. D. Egbert & Erofeeva, 2002) barotropic tidal forcing at the boundary. The second set (smooth forcing; herein after SM) has no tidal forcing, and the high frequency component of the wind forcing and boundary conditions are removed, using a low-pass filter with a one-day width, to eliminate IWs. The third set (no tidal forcing; herein after NT) has hourly wind- and boundary-forcing but no tidal forcing, and is only simulated on the 2 km grid. The outermost nest is run for three years beginning on 1 January, 1999 with the first two years used for spin-up and only the last year used to force the finer nests. All simulation sets are subsequently run for a full year beginning on 1 January, 2001. We focus our analysis on winter months (January, February, March) and summer months (July, August, September) and use hourly output fields.

Because our modeling approach has no data assimilation our solutions should be viewed as realistic process studies and validation against data can only be done in a statistical sense. With that in mind, the model's annual-mean mesoscale geostrophic eddy kinetic energy at the surface compares well with the Archiving, Validation, and Interpretation of Satellite Oceanographic (AVISO) data set (Fig. 1c,d; SI-Comparison with measurements), where measured monthly data spanning 1992-2009 is used. Similarly,

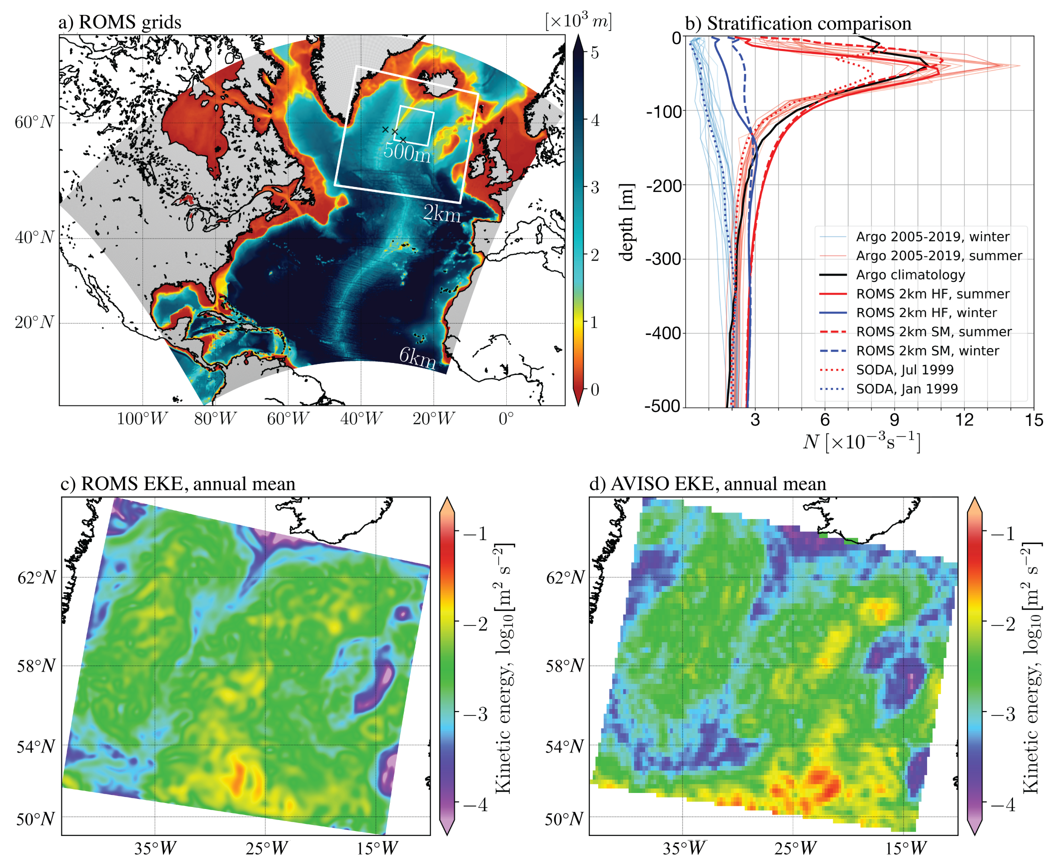

Figure 1. a) the ROMS grids used in this study (6 km, 2 km, and 500 m horizontal grid spacing) with colors showing bathymetry and markers indicating mooring locations. b) Horizontally- and seasonally-averaged stratification comparison between the ROMS 2 km solutions (thick solid and dashed red and blue lines), Argo-based profiles during 2005-2019 (thin solid red and blue lines), Argo annual climatology from the world-ocean atlas (solid black line), and the SODA product (dotted red and blue lines) used to initialize the 6 km solution. c) ROMS 2km HF solution-based and d) AVISO-based annual mean surface geostrophic eddy kinetic energy (EKE; where 'eddy' denote a perturbation from annual mean), displayed with a log-scale colorbar. The horizontal mean and standard deviation of EKE based on AVISO data from 1992-2009 is $3.41 \pm 0.47 \times 10^{-3} m^2 s^{-2}$ and based on ROMS from 2001 is $3.18 \pm 0.27 \times 10^{-3} m^2 s^{-2}$. HF and SM denote solutions with and without IW forcing, respectively. Further information about the data product and methods is provided in SI-Comparison with measurements.

the horizontally- and seasonally-averaged stratification in the model compare well with Argo-based measurements, which span 2005-2019 (Fig. 1b; SI-Comparison with measurements), although in winter the model is somewhat more stratified than the observations. The averaged stratification from the Simple Ocean Data Assimilation (SODA; Carton & Giese, 2008) product used to initialize the coarsest solution is also shown for reference (dotted red and blue lines in Fig. 1b).

To further examine how well the model captures the KE distribution as a function of time scales and depth we compare the model power spectral densities (Fig. 2) with mooring based measurements (crosses in Fig. 1a, SI-Comparison with measurements), which were collected during the Reykjanes Ridges Experiment (Vic et al., 2021). Considering the differences in measured vs. simulated years, the model does well at capturing low-frequency (mesoscale) variability as well as the near-inertial and semidiurnal tidal peaks (solid and dashed red lines in Fig. 2), which are the main focus of this manuscript. The submesoscale energy levels (time scales of about a day) are also well represented, particularly in the 500 m nest (dashed red lines in Fig. 2). The model, however, underestimates the IW continuum energy, probably due to the lack of vertical and horizontal resolution and/or the exclusion of remotely generated internal tides (Nelson et al., 2020). The model is also missing a diurnal tidal peak during summer at depth (Fig. 2e,f), which is presumably associated with the near-ridge dynamics. We do not expect these discrepancies to influence our results, which are focused on the bulk eddy-IW energy exchanges in this region.

3 Cross-scale energy transfers

The frequency spectra of the SM 2 km and 500 m solutions show a substantial energy reduction in time scales shorter than a day compared with HF solutions during both winter and summer[1] (red and green lines in Fig. 2), as expected from solutions that lack IW forcing.

In addition, a closer look at the frequency spectra at mesoscale time scales (of order 7-10 days) reveals a reduction in energy levels in the HF solutions compared with the SM solutions, at both resolutions. Using a one-week filter cutoff, the seasonal- and volume-averaged low-passed KE in the 2 km HF solution are 12% and 16% less than in the 2 km SM solution in winter and summer, respectively. The reduction in low-passed KE in the 500 m HF solution in both seasons increases to about 24% compared with the 500 m SM solution. We compared the domain averaged low-passed wind work between the HF and SM solutions and found little differences, with a somewhat larger low-passed wind input in the HF solutions (SI-Energetics). This verifies that the reduction in mesoscale KE is not related to differences in the atmospheric forcing. Furthermore, the mesoscale KE estimates above are computed over the region occupied by the 500 m grid (Fig. 1a) and depth averaged only over the top 500 m, because this is the modeled region that was best validated with respect to observations. It is noteworthy that the KE reduction is larger in the 2 km HF solution (up to $\approx 40\%$ during summer) if we pick the entire 2 km domain (SI-Energetics), suggesting that the reported values are quite conservative.

The observed reduction in mesoscale KE is a major finding of this study and our goal is to test whether it is induced by IWs. To this end we evaluate the physical-space, temporal scale-to-scale KE transfer rate in all of our solutions using the coarse-graining approach (Germano, 1992; Eyink, 2005; Aluie et al., 2018). This method is advantageous in comparison to the more commonly used spectral methods because it does not require windowing nor the assumptions of homogeneity or isotropy. In addition, the approach

[1] the inertial peak in the SM solutions is not completely eliminated, however the energy levels are 1-2 orders of magnitude smaller compared with the HF solutions.

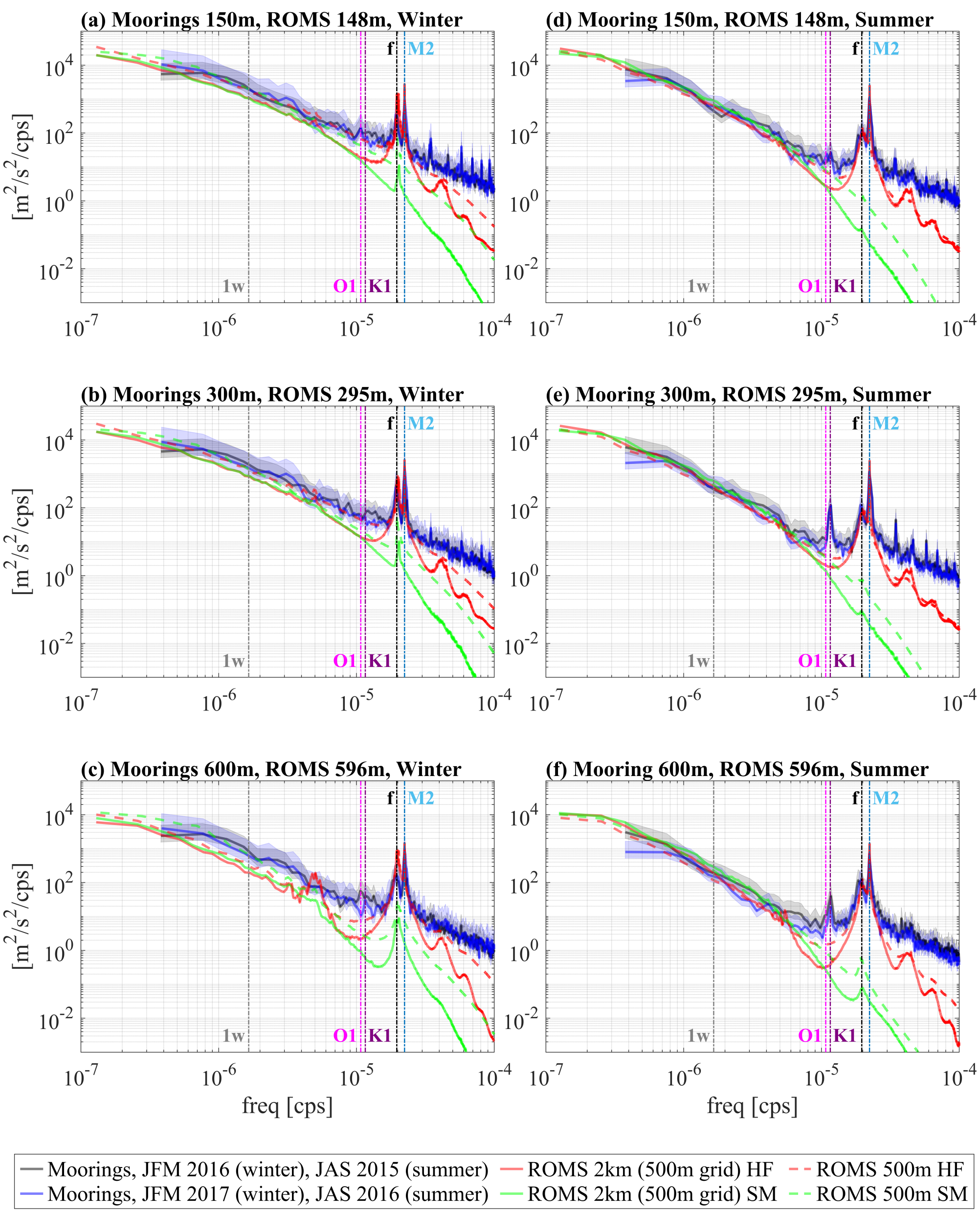

Figure 2. Power spectral densities of horizontal velocities from the mooring data and from the ROMS 2 km and 500 m solutions computed during winter (panels a-c) and summer (panels d-f), at three different depths. The mooring-based spectral densities (black and blue lines) use five overlapping segments with a 50% overlap and are averaged between the three moorings (markers in Fig. 1a) separately for each season, where the shading denotes the 95% confidence interval (SI- Comparison with measurements). The ROMS-based spectral densities for both the 2 km and 500 m solutions are averaged over the region occupied by the 500 m grid (Fig. 1a). The vertical dashed lines denote one week (1w), the diurnal and semi-diurnal tidal constituents (O1,K1, M2), and the inertial frequency (f). HF and SM denote solutions with and without IW forcing, respectively.

is Galilean invariant and therefore less susceptible to doppler-shifting effects and, because it relies on the use of filters in physical space, can also provide structural information about the flow features where the energy transfers take place (e.g. Schubert et al., 2020). A temporal-based analysis is chosen (e.g., Barkan et al., 2017) because the time scales of mesoscale motions and IWs are unambiguously distinguishable, whereas the spatial scales are not.

We compute the coarse-grained KE flux, Π_τ, across a temporal scale τ using (e.g., Aluie et al., 2018)

$$\Pi_\tau(\boldsymbol{x}, t) = -\left(\overline{u_i u_j}^\tau - \overline{u_i}^\tau \overline{u_j}^\tau\right) \frac{\partial \overline{u_i}^\tau}{\partial x_j}, \tag{1}$$

where $\overline{()}^\tau$ denotes the width of a low-passed filter applied to the three dimensional velocity field $(u_1, u_2, u_3) = (u, v, w)$; $\boldsymbol{x} = (x_1, x_2, x_3) = (x, y, z)$ is the three dimensional position vector; $i = 1, 2$; $j = 1 - 3$; and summation over repeated indices is assumed. To avoid the edge effects associated with the filtering procedure, the beginning- and end-period corresponding to $1.5\times\tau$ are discarded from the computation. By systematically varying τ we obtain the temporal KE fluxes as a function of filter width, where positive (negative) Π_τ values indicate a forward (inverse) energy transfer across a scale τ. In what follows τ has units of hours and Π_τ is plotted as a function of the equivalent frequency $1/\tau$, so that the coarse-grained KE fluxes can be interpreted in the same way as the more commonly used spectral KE fluxes (e.g., Arbic et al., 2012).[2]

The shape of the depth integrated and horizontally- and seasonally-averaged Π_τ in all solutions shows that there are scale ranges with both an inverse and a forward energy cascade with intersection periods that vary between approximately 1-3 days, depending on the solution (Fig. 3a,b). A comparison between the SM and HF solutions (solid/dashed black and blue lines in Fig. 3a,b) demonstrates that IW forcing enhances the forward cascade and reduces the inverse cascade in all cases, where the absolute differences between the HF and SM flux values are as large as the flux magnitudes in the SM solutions. There are some variations in Π_τ between the NT and HF solutions, particularly during summer (magenta and black lines in Fig. 3b), but qualitatively the induced scale-to-scale flux changes seem to be primarily associated with high-frequency wind forcing and the excitation of NIWs. In most HF solutions there is a local minimum around the inertial frequency (solid red line in Fig. 3a,b), indicative of a source of NI energy, followed by a local maximum at super-inertial frequencies. This local maximum may be associated with a direct (i.e., non-cascading) KE transfer from mesoscale to IW time scales, as suggested by previous theories (e.g., Xie & Vanneste, 2015). At sub-inertial frequencies, however, the externally forced IWs seem to affect the energetics by modifying the turbulent cascades. This cascade-modifying process was termed *stimulated* cascade in Barkan et al. (2017), and was since discussed in Xie (2020) and J. Thomas & Daniel (2021).

Most strikingly, the KE transfer to super-inertial frequencies in the winter 500 m HF solution is substantially larger than that of the winter 500 m SM solution (dashed black and blue lines in Fig. 3a), and is on the order of $1\,\mathrm{mW/m^2}$. This is comparable to the horizontally-averaged NI wind work in this region $\boldsymbol{u}_\mathrm{s}^{\mathrm{NI}} \cdot \boldsymbol{\mathcal{T}}^{\mathrm{NI}}$, where $\boldsymbol{u}_\mathrm{s}$ is the horizontal surface velocity vector, $\boldsymbol{\mathcal{T}}$ is the surface wind stress vector, and NI denotes a band-pass filter in the $[0.9f, 1.1f]$ frequency band, with f denoting the domain-averaged Coriolis frequency in the 500 m grid. The depth structure of the coarse-grained KE fluxes in the 500 m solutions indicates that transfers are primarily confined to the mixed layer during winter (Fig. 3c,e), and extend below the mixed layer during summer (Fig. 3d,f). This suggests that during winter the majority of the transfers may be associated with

[2] the analogy between coarse-grained and spectral fluxes requires the use of a spectrally-sharp filter, like the 6^{th} order Butterworth filter used in our analysis.

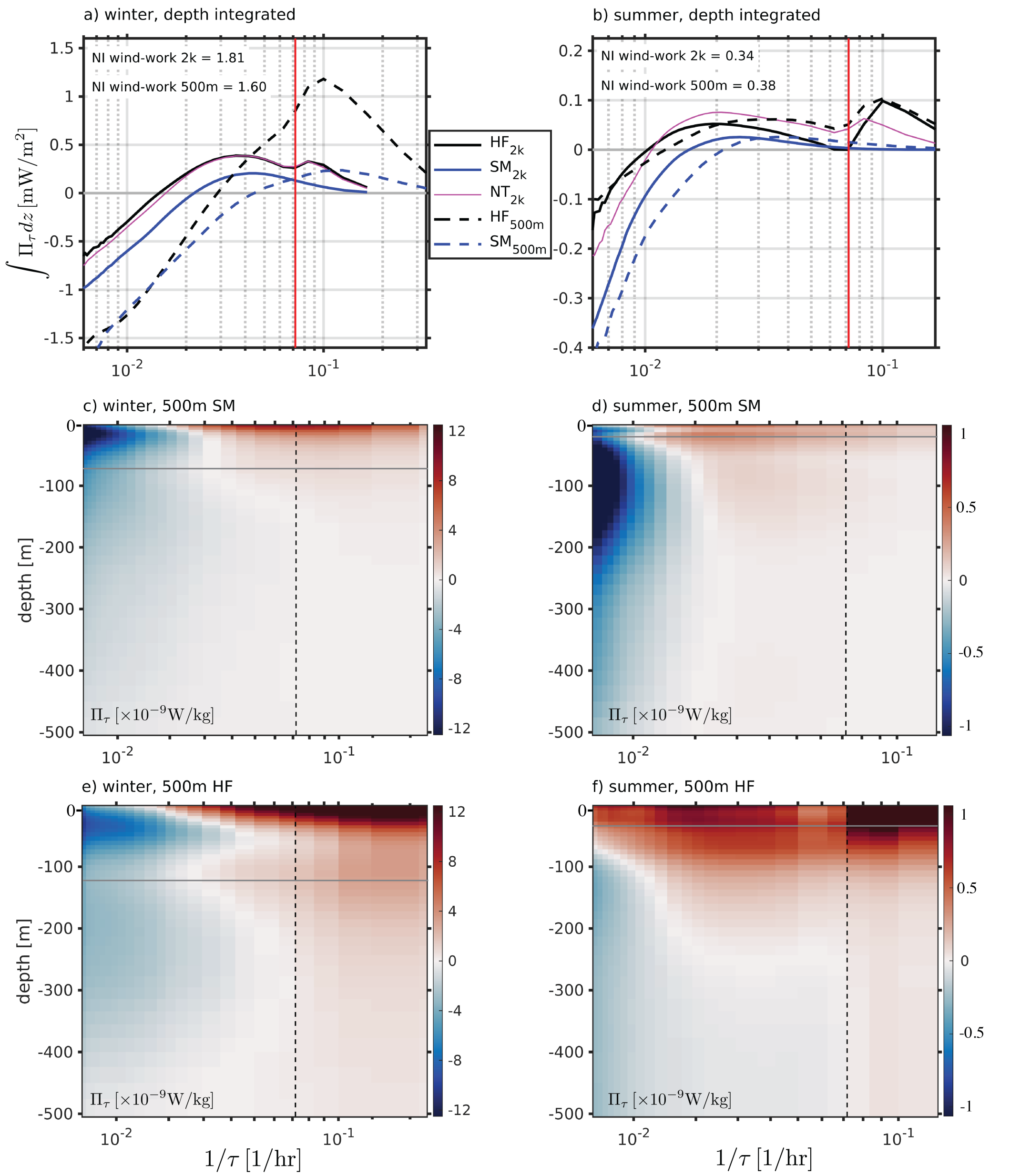

Figure 3. a,b) Depth integrated (over the top 500 m) and seasonally- and horizontally-averaged coarse-grained KE fluxes, Π_τ, for all numerical simulations described in the text, where temporal filters are computed using a 6th order Butterworth filter. c-f) The depth structure of the seasonally- and horizontally-averaged Π_τ for the 500 m solutions. HF and SM denote solutions with and without IW forcing, respectively. NT denotes a solution with high-frequency wind forcing but without tidal forcing. Vertical lines (red in panels a,b and dashed black in panels c-f) denote the inertial frequency. Horizontal grey lines in panels c-f denote the seasonally- and horizontally-averaged mixed layer depth based on the 0.03 kg/m^3 density criterion (de Boyer Montégut et al., 2004). Horizontal averages are taken over the region occupied by the 500 m grid (Fig. 1a). The seasonally- and horizontally-averaged near-inertial (NI) wind work (in mW/m^2) for the HF 500 m and 2 km solutions are marked in panels a and b.

surface intensified submesoscale currents whereas during summer they are largely linked to mesoscale motions, which typically extend deeper into the thermocline.

4 Flow structures

The substantial increase in forward KE fluxes to super-inertial frequencies during winter in the HF solutions, which is largely confined to the mixed layer and that increases with increasing model resolution (Fig. 3), suggests that submesoscale fronts and filaments, which are only adequately resolved in the 500 m solutions, play an important role in the interactions between eddies and internal wave.

To test this hypothesis we compute the integrated coarse-grained KE fluxes to super-inertial frequencies, Π_{14}, over the top 100 m (Fig. 4a), which is roughly the averaged mixed-layer depth during winter in the 500 m HF solution (Fig. 3e). Although the signal is somewhat noisy there is a visual correspondence between regions of strong and positive Π_{14} values and regions of strong fronts, which are defined as the ninetieth percentile of the horizontal buoyancy gradient magnitudes $|\nabla_n b|$ ($\approx 1 \times 10^{-7}\mathrm{s}^{-2}$; Fig. 4b). Quantitatively, Π_{14} averaged over frontal regions is positive and, in the upper 50 m, nearly an order of magnitude larger than the spatially averaged Π_{14} (Fig. 4c).

The frontal-averaged root-mean-squared vorticity and horizontal divergence values normalized by the local Coriolis frequency (rms(ζ/f) and rms(δ/f)) are no longer small in the upper 50 m, indicating a significant departure from geostrophy (Fig. 4d,e). This dynamical importance of ageostrophic motions is further confirmed by the frontal-averaged skewness values (solid blue lines in Fig. 4d,e), which are positive (negative) for ζ/f (δ/f), as expected from the circulations around submesoscale fronts and filaments (Capet et al., 2008b; Shcherbina et al., 2013; D'Asaro et al., 2018; Barkan et al., 2019). The importance of the interactions between submesoscale frontal structures and NIWs has been suggested before in theoretical and idealized numerical studies (L. N. Thomas, 2012; Whitt & Thomas, 2015; Barkan et al., 2017), but, to our knowledge, never before demonstrated and quantified in realistic simulations.

5 Implications

The above numerical results and analyses have important implications to dissipation routes of oceanic mesoscale KE and to the energization of NIWs, both of which can significantly affect climate equilibria and biogeochemistry. We offer two approaches to quantify these dissipation and energization processes globally. These approaches assume that the energy transfers in the region of study are representative of other ocean basins, which is difficult to evaluate, and therefore only provide order-of-magnitude estimates.

First, the difference in the magnitudes of the positive KE flux to super-inertial frequencies between the 500 m HF and SM solutions (Fig. 3a,b) can be multiplied by the surface area of the global world oceans to estimate the IW-induced forward cascade. This gives approximately 0.35 TW during winter and about a tenth of that during summer.

Second, the same flux magnitude differences between the 500 m HF and SM solutions can be divided by the regionally-averaged near-inertial wind work in each season to give the ratio between the super-inertial KE that is transferred from mesoscale motions to that generated by the wind. This ratio is about 0.5-0.6 during winter and 0.18-0.25 during summer. Assuming most of the KE exchanges are associated with NIWs, as indicated by the comparison between HF and NT solutions (Fig. 3a,b), we multiply these ratios by global estimates of the power input into near-inertial motions, which ranges between 0.3-1.3 TW (Jiang et al., 2005; Alford, 2020). This approximates the IW-induced

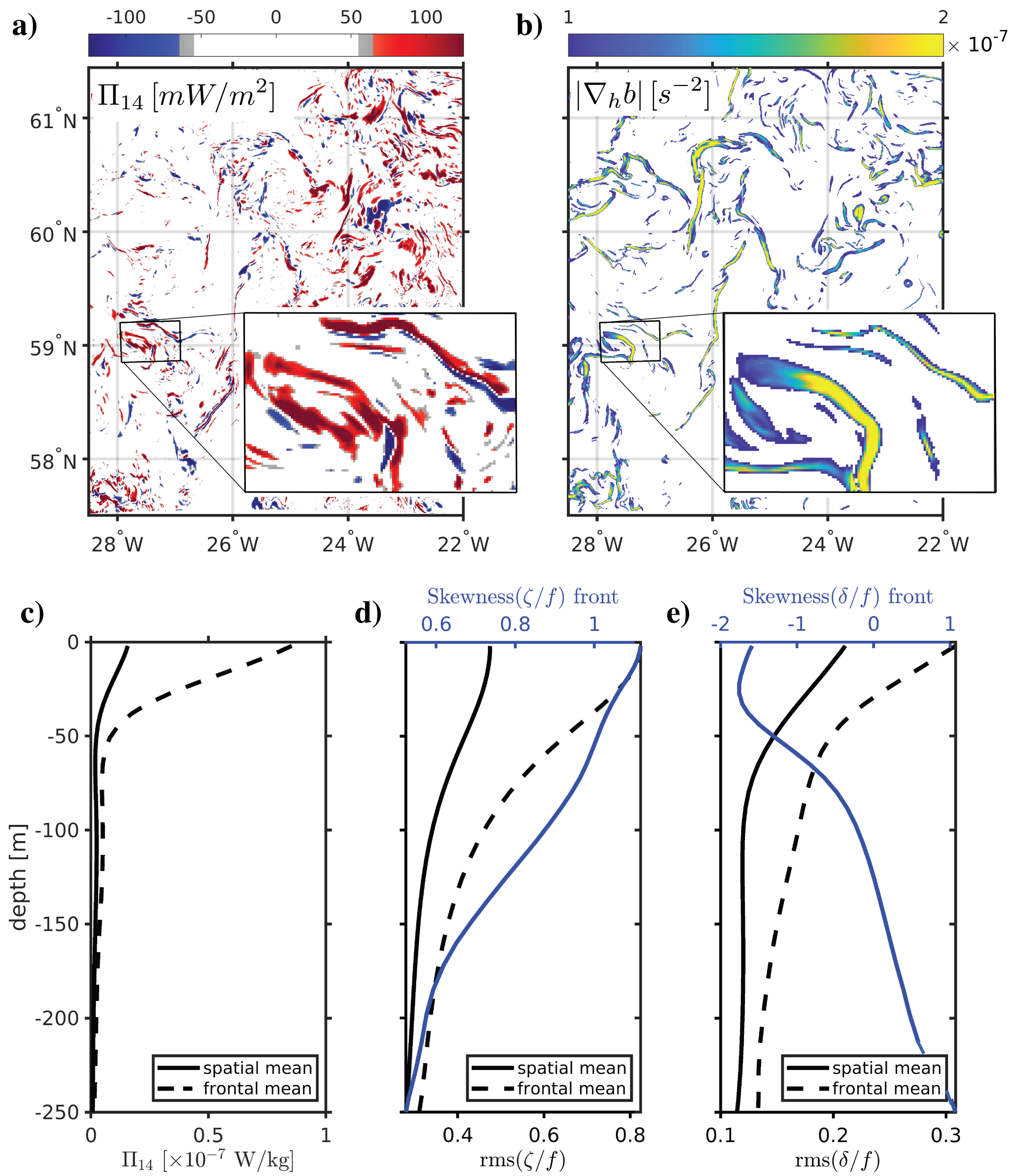

Figure 4. a) A representative snapshot of the coarse-grained KE flux to time scales shorter than 14 hours (the inertial period in this region) Π_{14}, depth integrated over the top 100 m. b) The 90th percentile of the horizontal buoyancy gradient magnitude $|\nabla_h b|$ (i.e., 'frontal regions') during the same snapshot as in panel a, low-passed with a 14 hour cutoff filter, and depth averaged over the top 100 m. Insets in panels a and b zoom-in on representative structures. Time-mean c) Π_{14}, d) root-mean-square vorticity normalized by the Coriolis frequency (rms(ζ/f)), and e) root-mean-square divergence normalized by the Coriolis frequency (rms(δ/f)), horizontally averaged over the entire 500m domain (solid black line) and over the 'frontal regions' (dashed black line). Blue lines in panels d and e show the skewness of ζ/f and δ/f, respectively, computed in the 'frontal regions'. All quantities are based on the 500 m HF solution, during winter.

forward cascade to be between 0.05-0.8 TW with an annual average of 0.3 TW.[3] Given that the reduction of low-passed mesoscale energy in the 2 km HF solution is larger when computed over the entire 2 km domain (SI-Energetics) and that the IW-induced decrease in the inverse KE cascade at sub-inertial frequencies is not taken into consideration in the estimates above, we believe these reported values to be rather conservative.

The strongest forward KE fluxes are found in winter at flow features that are characterized by strong buoyancy gradients and a significant departure from geostrophy (Fig. 4). We presume that it is at these submesoscale frontal structures that the KE energy exchanges are most likely to be observed *in situ*.

From a modeling perspective, numerical solutions that exclude IW forcing and/or lack the resolution to adequately resolve the flow structures where the energy transfers occur are expected to over-estimate the low-frequency mesoscale energy by as much as 25%. This over-estimate is comparable in magnitude to the one recently reported for current feedback effects (Renault et al., 2016) and can potentially have significant implications to climate models' predictability, in case they do not adequately represent these 'eddy-IW' interactions.

Admittedly, we do not offer here a mechanistic explanation for the stimulated reduction in the inverse KE transfer to sub-inertial frequencies and for the stimulated forward transfer to super-inertial frequencies. Nor do we provide a more in-depth spatiotemporal depiction of the KE energy transfers, following a decomposition between mesoscale, submesoscale, and IW motions. These endeavors are explored in detail in forthcoming publications.

Acknowledgments

RB, KS, LY, and JCM were supported by ONR-N000141812697. RB was further supported by NSF Grant OCE-1851397 and Israeli Science foundation Grant 1736/18. JCM was further supported ONR-N000141812599 and ONR N000142012023. J.G. gratefully acknowledges support from the French National Agency for Research (ANR) through the project DEEPER (ANR-19-CE01-0002-01). Information about how to access the mooring data can be found in Branellec & Thierry (2016, 2018).

References

Alford, M. H. (2003). Redistribution of energy available for ocean mixing by long-range propagation of internal waves. *Nature*, *423*(6936), 159–162.

Alford, M. H. (2020). Revisiting near-inertial wind work: Slab models, relative stress, and mixed layer deepening. *Journal of Physical Oceanography*, *50*(11), 3141–3156.

Alford, M. H., MacKinnon, J. A., Pinkel, R., & Klymak, J. M. (2017). Space–time scales of shear in the north pacific. *Journal of Physical Oceanography*, *47*(10), 2455–2478.

Alford, M. H., MacKinnon, J. A., Simmons, H. L., & Nash, J. D. (2016). Near-inertial internal gravity waves in the ocean. *Annu. Rev. Mar. Sci.*, *8*, 95-123. doi: 10.1146/annurev-marine-010814-015746

Aluie, H., Hecht, M., & Vallis, G. K. (2018). Mapping the energy cascade in the North Atlantic ocean: The coarse-graining approach. *Journal of Physical Oceanography*, *48*(2), 225–244.

Arbic, B. K., Scott, R. B., Flierl, G. R., Morten, A. J., Richman, J. G., & Shriver,

[3] based on an assumed 0.8TW power input into near-inertial motions and an annual-mean ratio of 0.375 between KE flux to super inertial motions and near-inertial wind work.

J. F. (2012). Nonlinear cascades of surface oceanic geostrophic kinetic energy in the frequency domain. *Journal of Physical Oceanography*, *42*, 1577–1600.

Arbic, B. K., Shriver, J. F., Hogan, P. J., Hurlburt, H. E., McClean, J. L., Metzger, E. J., ... Wallcraft, A. J. (2009). Estimates of bottom flows and bottom boundary layer dissipation of the oceanic general circulation from global high-resolution models. *Journal of Geophysical Research: Oceans*, *114*.

Barkan, R., Molemaker, M. J., Srinivasan, K., McWilliams, J. C., & D'Asaro, E. A. (2019). The role of horizontal divergence in submesoscale frontogenesis. *Journal of Physical Oceanography*, *49*(6), 1593–1618.

Barkan, R., Winters, K. B., & McWilliams, J. C. (2017). Stimulated imbalance and the enhancement of eddy kinetic energy dissipation by internal waves. *J. Phys. Oceanogr.*, *47*, 181–198.

Branellec, P., & Thierry, V. (2016). Rrex 2015. ctd-o2 data report. *ODE/LOPS/16-26*.

Branellec, P., & Thierry, V. (2018). Rrex 2017. ctd-o2 data report. *Rap. Int. LOPS/18-04*.

Bühler, O., & McIntyre, M. E. (2005). Wave capture and wave–vortex duality. *Journal of Fluid Mechanics*, *534*, 67–95.

Capet, X., McWilliams, J. C., Molemaker, M. J., & Shchepetkin, A. F. (2008a). Mesoscale to submesoscale transition in the California Current System. Part i: Flow structure, eddy flux, and observational tests. *J. Phys. Oceangr.*, *38*, 29–43.

Capet, X., McWilliams, J. C., Molemaker, M. J., & Shchepetkin, A. F. (2008b). Mesoscale to submesoscale transition in the California Current System. Part ii: Frontal processes. *J. Phys. Oceangr.*, *38*, 44–64.

Carton, J. A., & Giese, B. S. (2008). A reanalysis of ocean climate using simple ocean data assimilation (soda). *Monthly weather review*, *136*(8), 2999–3017.

Chaigneau, A., Pizarro, O., & Rojas, W. (2008). Global climatology of near-inertial current characteristics from lagrangian observations. *Geophys. Res. Letts.*, *35*.

D'Asaro, E. A., Shcherbina, A. Y., Klymak, J. M., Molemaker, J., Novelli, G., Guigand, C. M., ... others (2018). Ocean convergence and the dispersion of flotsam. *Proceedings of the National Academy of Sciences*, *115*(6), 1162–1167.

de Boyer Montégut, C., Madec, G., Fischer, A. S., Lazar, A., & Iudicone, D. (2004). Mixed layer depth over the global ocean: An examination of profile data and a profile-based climatology. *J. Geophy. Res.: Oceans*, *109*(C12).

Dee, D., Balmaseda, M., Balsamo, G., Engelen, R., Simmons, A., & Thépaut, J.-N. (2014). Toward a consistent reanalysis of the climate system. *Bulletin of the American Meteorological Society*, *95*(8), 1235–1248.

Egbert, G., & Ray, R. (2000). Significant dissipation of tidal energy in the deep ocean inferred from satellite altimeter data. *Nature*, *405*(6788), 775–778.

Egbert, G. D., Bennett, A. F., & Foreman, M. G. (1994). Topex/poseidon tides estimated using a global inverse model. *Journal of Geophysical Research: Oceans*, *99*(C12), 24821–24852.

Egbert, G. D., & Erofeeva, S. Y. (2002). Efficient inverse modeling of barotropic ocean tides. *Journal of Atmospheric and Oceanic technology*, *19*(2), 183–204.

Eyink, G. L. (2005). Locality of turbulent cascades. *Physica D: Nonlinear Phenomena*, *207*(1-2), 91–116.

Fratantoni, D. M. (2001). North Atlantic surface circulation during the 1990's observed with satellite-tracked drifters. *J. Geophys. Res.: Oceans*, *106*, 22067–22093.

Germano, M. (1992). Turbulence- the filtering approach. *Journal of Fluid Mechanics*, *238*(1), 325–336.

Jakobsen, P. K., Ribergaard, M. H., Quadfasel, D., Schmith, T., & Hughes, C. W. (2003). Near-surface circulation in the northern North Atlantic as inferred from lagrangian drifters: Variability from the mesoscale to interannual. *J. Geophys.*

Res.: Oceans, *108*.

Jiang, J., Lu, Y., & Perrie, W. (2005). Estimating the energy flux from the wind to ocean inertial motions: The sensitivity to surface wind fields. *Geophys. Res. Letts.*, *32*(15).

Jochum, M., Briegleb, B. P., Danabasoglu, G., Large, W. G., Norton, N. J., Jayne, S. R., ... Bryan, F. O. (2013). The impact of oceanic near-inertial waves on climate. *Journal of Climate*, *26*(9), 2833–2844.

McWilliams, J. C. (2016). Submesoscale currents in the ocean. In *Proc. r. soc. a* (p. 20160117).

Müller, P., McWilliams, J. C., & Molemaker, M. J. (2005). Routes to dissipation in the ocean: The 2d/3d turbulence conundrum. In H. B. J. Simpson & J. Sündermann (Eds.), *Marine turbulence* (pp. 397–405). Cambridge University Press.

Nelson, A., Arbic, B., Menemenlis, D., Peltier, W., Alford, M., Grisouard, N., & Klymak, J. (2020). Improved internal wave spectral continuum in a regional ocean model. *Journal of Geophysical Research: Oceans*, *125*(5), e2019JC015974.

Nikurashin, M., Vallis, G. K., & Adcroft, A. (2013). Routes to energy dissipation for geostrophic flows in the southern ocean. *Nature Geoscience*, *6*, 48–51.

Pinkel, R. (2014). Vortical and internal wave shear and strain. *Journal of physical oceanography*, *44*, 2070–2092.

Polzin, K. L. (2010). Mesoscale eddy-internal wave coupling. part ii: Energetics and results from polymode. *J. Phys. Ocean.*, *40*(4), 789–801.

Renault, L., Molemaker, M. J., McWilliams, J. C., Shchepetkin, A. F., Lemarié, F., Chelton, D., ... Hall, A. (2016). Modulation of wind work by oceanic current interaction with the atmosphere. *J. Phys. Oceanogr.*, *46*, 1685–1704.

Rocha, C. B., Wagner, G. L., & Young, W. R. (2018). Stimulated generation: Extraction of energy from balanced flow by near-inertial waves. *Journal of Fluid Mechanics*, *847*.

Schubert, R., Gula, J., Greatbatch, R. J., Baschek, B., & Biastoch, A. (2020). The submesoscale kinetic energy cascade: Mesoscale absorption of submesoscale mixed layer eddies and frontal downscale fluxes. *Journal of Physical Oceanography*, *50*(9), 2573–2589.

Sen, A., Scott, R. B., & Arbic, B. K. (2008). Global energy dissipation rate of deep-ocean low-frequency flows by quadratic bottom boundary layer drag: Computations from current-meter data. *Geophysical Research Letters*, *35*.

Shchepetkin, A. F., & McWilliams, J. C. (2005). The Regional Oceanic Modeling System: A split-explicit, free-surface, topography-following-coordinate oceanic model. *Ocean Modelling*, *9*, 347–404.

Shcherbina, A. Y., D'Asaro, E. A., Lee, C. M., Klymak, J. M., Molemaker, M. J., & McWilliams, J. C. (2013). Statistics of vertical vorticity, divergence, and strain in a developed submesoscale turbulence field. *Geophys. Res. Lett.*, *40*, 4706–4711.

Taylor, S., & Straub, D. (2016). Forced near-inertial motion and dissipation of low-frequency kinetic energy in a wind-driven channel flow. *J. Phys. Oceanogr.*, *46*(1), 79–93.

Thomas, J., & Daniel, D. (2020). Turbulent exchanges between near-inertial waves and balanced flows. *Journal of Fluid Mechanics*, *902*(LA-UR-19-32700).

Thomas, J., & Daniel, D. (2021). Forward flux and enhanced dissipation of geostrophic balanced energy. *Journal of Fluid Mechanics*, *911*.

Thomas, L. N. (2012). On the effects of frontogenetic strain on symmetric instability and inertia-gravity waves. *J. Fluid Mech.*, *711*, 620–640.

Thomas, L. N. (2017). On the modifications of near-inertial waves at fronts: implications for energy transfer across scales. *Ocean Dynamics*, *67*(10), 1335–1350.

Thomas, L. N., Rainville, L., Asselin, O., Young, W. R., Girton, J., Whalen, C. B., ... Hormann, V. (2020). Direct observations of near-inertial wave ζ-refraction in a dipole vortex. *Geophysical Research Letters*, *47*(21), e2020GL090375.

Trossman, D. S., Arbic, B. K., Garner, S. T., Goff, J. A., Jayne, S. R., Metzger, E. J., & Wallcraft, A. J. (2013). Impact of parameterized lee wave drag on the energy budget of an eddying global ocean model. *Ocean Modelling*, *72*, 119–142.

Trossman, D. S., Arbic, B. K., Richman, J. G., Garner, S. T., Jayne, S. R., & Wallcraft, A. J. (2016). Impact of topographic internal lee wave drag on an eddying global ocean model. *Ocean Modelling*, *97*, 109–128.

Vic, C., Ferron, B., Thierry, V., Mercier, H., & Lherminier, P. (2021). Tidal and near-inertial internal waves over the Reykjanes Ridge. *Journal of Physical Oceanography*, *51*(2), 419–437.

Wagner, G., & Young, W. (2016). A three-component model for the coupled evolution of near-inertial waves, quasi-geostrophic flow, and the near-inertial second harmonic. *J. Fluid. Mech.*, *11*, 1111.

Whitt, D. B., & Thomas, L. N. (2015). Resonant generation and energetics of wind-forced near-inertial motions in a geostrophic flow. *J. Phys. Oceanogr.*, *45*(1), 181–208.

Wunsch, C., & Ferrari, R. (2004). Vertical mixing, energy, and the general circulation of the oceans. *Ann. Rev. Fluid Mech.*, *36*, 281–314.

Xie, J.-H. (2020). Downscale transfer of quasigeostrophic energy catalyzed by near-inertial waves. *Journal of Fluid Mechanics*, *904*, A40.

Xie, J.-H., & Vanneste, J. (2015). A generalised-lagrangian-mean model of the interactions between near-inertial waves and mean flow. *Journal of Fluid Mechanics*, *774*, 143–169.

Supporting Information for "Oceanic mesoscale eddy depletion catalyzed by internal waves"

Roy Barkan[1,2], Kaushik Srinivasan[2], Luwei Yang[2], James C. McWilliams[2],

Jonathan Gula[3,4], Clément Vic[3]

[1]Porter School of the Environment and Earth Sciences, Tel Aviv University, Ramat Aviv, Israel 6997801

[2]Department of Atmospheric and Oceanic Sciences, University of California, Los Angeles, CA 90095

[3]Laboratoire d'Océanographie Physique et Spatiale, Université de Bretagne Occidentale, Plouzané, France 29280

[4]Institut Universitaire de France (IUF)

Contents of this file

1. Text S1 to S3
2. Figures S1 to S6
3. Tables S1

Corresponding author: R. Barkan, Porter School of the Environment and Earth Sciences, Tel Aviv University, Ramat Aviv, Israel 6997801, and Department of Atmospheric and Oceanic Sciences, University of California, Los Angeles, CA 90095, USA. (rbarkan@tauex.tau.ac.il)

Introduction

The supporting information provides details about the modeling approach and setup, including the required parameters to reproduce the numerical solutions described in the manuscript. In addition, it provides detailed information about the various data sets and analysis methods used to compare between model solutions and *in-situ* measurements. Finally, it provides additional figures and discussion to complement and support the energetic analysis shown in the main manuscript.

S1: Modelling

All simulations are carried out using the Regional Oceanic Modeling System (ROMS; Shchepetkin & McWilliams, 2005), which solves the Primitive Equations in terrain following coordinates using the full equation of state for seawater (Shchepetkin & McWilliams, 2011). We utilize a one-way nesting procedure as described in Mason et al. (2010) with successive, nearly isotropic ($dx \approx dy$) grid resolutions, varying from $\approx$ 6 km covering most of the Atlantic Ocean, $\approx$ 2 km for the North Atlantic Subpolar Gyre region, and $\approx$ 500 m for the Iceland basin (Figure 1a). The stretching parameters for all simulations are H_{cline}=350m, $\theta_s = 6$, $\theta_b = 4.5$. The number of sigma levels used is 50, 100, and 150 for the 6 km, 2km, and 500 m nests, respectively. For the 2 km (500 m) solution analyzed in this manuscript, assuming a water depth of 3 km, the above parameters correspond to vertical resolution of approximately 3 m (2 m) near the surface, which gradually decays down to approximately 26 m (17 m) at 500 m depth. The bathymetry for all domains is constructed from the SRTM30_PLUS dataset (available at http://topex.ucsd.edu/WWW_html/srtm30_plus.html) and is smoothed to avoid aliasing whenever the bathymetric data are available at higher resolution than the computation grid (e.g. Lemarié et al., 2012). The boundary conditions for the outermost nest are from the Simple Ocean Data Assimilation (SODA; Carton & Giese, 2008), and atmospheric forcing is from the Climate Forecast System Reanalysis (CFSR) atmospheric product (Dee et al., 2014) with hourly temporal resolution. The surface turbulent evaporation, heat, and momentum fluxes are estimated using bulk formulae (W. B. Large, 2006), and take into account ocean current feedback effects (e.g. Renault et al., 2016). TPXO-based (Egbert et al., 1994; Egbert & Erofeeva, 2002) barotropic tidal forcing is applied at the boundary of the 2 km nest. In the analyzed solutions the vertical mixing of tracers and momentum at the surface and bottom boundary layers is done with the K-profile parametrization (KPP) (W. G. Large et al., 1994). A third order horizontal upstream-biased advection scheme, which implicitly works as a horizontal mixing parametrization for momenta and tracers, is used and augmented by the vertical semi-implicit advection scheme discussed in Shchepetkin (2015). Solutions forced by both hourly winds, hourly boundary forcing, and barotropic tides are called high-frequency (HF). Solutions forced by hourly winds and hourly boundary forcing but without barotropic tidal forcing are called no-tides (NT). Solutions without barotropic tidal forcing and with smoothed wind and boundary forcing are called smooth (SM). The smoothing in the SM solutions for both the wind velocities at 10 m and the boundary files is carried out using a Gaussian low-pass filter with a filter width of 24 hours.

S2: Comparison with measurements

Power spectral densities comparison with Mooring data

The moorings used for comparison with the model's power spectral densities are the Irminger West (IRW), the Reykjanes Ridge Top (RRT), and the Iceland East (ICE), located at (33.259°W, 59.091°N), (30.669°W, 58.773°N), and (28.447°W, 57.58°N), respectively. They were deployed on 16 - 28 June 2015 and recovered on 23 - 28 July 2017 (see cruise reports Branellec & Thierry, 2016, 2018 for details on the operations), and were designed to investigate internal wave activity in the cross-ridge direction (Vic et al., 2021). The data used in this study are from Teledyne WorkHorse acoustic Doppler current profilers (ADCPs) and Aanderaa Doppler and Nortek Aquadopp current meters. The 75-kHz (150-kHz) ADCPs recorded horizontal velocity every 180 s (30 s) with 16 m (8 m) vertical bins, using a single ping per ensemble to save up energy for the long-term deployment. Aanderaa and Aquadopp current meters recorded velocity every 600 s and 3600 s, respectively. Data quality was overall good except for short-term periods when measurements done by the upward-looking ADCPs close to the surface were contaminated by surface wave-induced signals. Those data were flagged and discarded from the analysis. Data was linearly interpolated on the vertical on an 8-m grid.

Only the data at depths 150 m, 300 m, and 600 m are used for validation. The data below that depth are not used because we suspect that the model KE is not yet equilibrated below this depth. Because the majority of the interactions and KE differences are largely confined to the upper 200 m, we do not believe that this potential lack of equilibration below 600 m depth should affect the results presented in this manuscript.

The power spectral densities from the mooring data are averaged over the three moorings in each season. To increase the number of degrees of freedom each time series was divided into 5 segments with a 50% overlap. The shading in Figure 2 represents the 95% confidence interval based on 30 degrees of freedom. The exception is the power spectral densities for winter 2016, where only two moorings were used (20 degrees of freedom) due to some missing data. The temporal power spectral densities from the model solutions were computed for winter and summer months at every point in the domain occupied by the 500 m grid (Fig. 1a) and then spatially averaged.

Geostrophic eddy kinetic energy comparison with AVISO

The seasonal and annual geostrophic eddy kinetic energy in ROMS was computed from the sea-surface-height field of the 2 km HF solution, where 'eddy' is defined as the perturbation from an annual mean. In order to compare the model results to the Archiving, Validation, and Interpretation of Satellite Oceanographic Data (AVISO) dataset (Ducet et al., 2000), we computed the geostrophic eddy kinetic energy from the sea surface height of the model, which was smoothed using a spatial two-dimensional Gaussian low-pass filter with a filter width of 40 km, and a temporal low-pass Gaussian filter with a filter width of 1 week.

Stratification comparison with Argo

The Argo (Argo, 2000) stratification data was computed based on profiles collected during winter and summer months between 2005 and 2019. The stratification estimates were obtained from the 1×1 degree variational interpolated monthly mean (http://apdrc.soest.hawaii.edu/projects/Argo/data/gridded/On_standard_levels/index1.html).

The Argo climatology is based on the World Ocean Atlas inferred statistics that can be downloaded at https://www.seanoe.org/data/00612/72432/. Figure S1 shows a comparison between the Argo-based and the model-based stratification estimates for the 2 km and 500 m domains.

S3: Energetics

Mesoscale energy computation

Figures S2 and S3 display the depth structure of the horizontally-averaged low-passed mesoscale KE from the 2 km and 500 m solutions, respectively. For both solutions the spatial average is done over the region occupied by the 500 m domain (Fig. 1a) and a 6th order Butterworth filter with a 1 week filter width is used for low-passing. The numbers in the bottom left corner of each panel indicate the seasonal- and depth-averaged low-passed KE over the top 500 m, and are summarized in Table S1. We verified that the differences in the low-passed energies are not associated with differences in the seasonal-mean KE, which are an order of magnitude smaller than the values reported here (not shown). For the 2 km solution, if we spatially average over the entire domain and not only the region occupied by the 500 m grid (Table S1), the KE reductions in the HF solution become 24% and 38% for winter and summer, respectively. These regional variations in the low-passed KE suggest that the results reported in the manuscript, which focus on the 500 m grid, are rather conservative.

Wind-work computation

The wind forcing in the model solutions is applied using a bulk formula, and the implementation takes into account current feedback effects (see SI-Modeling). Therefore, we cannot filter the wind stresses directly and instead, to generate SM solutions without NIW forcing, we filter the atmospheric wind velocities at 10 m height. Consequently, it is important to verify that the changes in the low-passed KE shown in Figs. S2 and S3 are not because of the modifications to the wind forcing. To this end we compute the seasonally- and horizontally-averaged low-passed and high-passed wind work $\boldsymbol{u}_s^{\mathrm{LP}} \cdot \boldsymbol{\mathfrak{T}}^{\mathrm{LP}}$ and $\boldsymbol{u}_s^{\mathrm{HP}} \cdot \boldsymbol{\mathfrak{T}}^{\mathrm{HP}}$ (Fig. S4). Above, $\boldsymbol{u}_s$ is the horizontal velocity vector at the surface, $\boldsymbol{\mathfrak{T}}$ is the surface wind stress vector, and LP and HP denote low-pass and high-pass filters, respectively, using a one week filter width. As shown in Fig. S4a,b, the low-passed wind work in the HF and SM solutions is quite similar during both seasons and, separately, between the 2 km and between the 500 m solutions. The differences between the 2 km and 500 m solutions (e.g., around day 25 in Fig. S4a) are a result of averaging over different domains. Quantitatively, there is more low-passed wind work in the HF solutions compared with the SM solutions, which is the opposite trend to that shown by the low-frequency KE values (Figs. S2 and S3, and Table S1). This shows that the reported reduction in low-passed KE cannot be explained by wind-work differences. The high-passed wind work (Fig. S4c,d) is displayed for completeness, and shows a substantial magnitude reduction in the SM solutions, as expected.

Cross-scale transfers in the 2 km solutions

Figure 3 (panels c-f) shows the depth structure of the spatially- and seasonally-averaged coarse-graining KE fluxes as a function of depth for the 500 m solutions. For completeness we show here the depth structure of the coarse-graining KE fluxes for the 2 km solutions (Fig. S5), where spatial averages are computed over the region occupied by the 500 m grid (Fig. 1a). Qualitatively, the signals are similar between the 500 m and 2 km solutions, however quantitatively the flux magnitudes are stronger in the 500 m solutions, particularly during winter. Similar patterns are found when the KE fluxes are computed over the entire 2 km domain (not shown), however the decrease in the inverse cascade magnitudes at low frequencies in the HF solution (compared with the SM solution) and the increase in the forward cascade magnitudes at super-inertial frequencies is larger when averages are taken over the entire 2 km domain. This explains why the integrated differences in the low-passed KE between the 2 km HF and SM solutions discussed above are larger when averaged over the entire 2 km domain.

Flow structures in the 500 m SM solution

Figure 4 quantifies the flow structures where the forward KE fluxes to super-inertial frequencies take place in the 500 m HF solution during winter. For completeness we show here the same analysis carried out for the 500 m SM solution during winter (Fig. S6). Similarly to the HF solution (Fig. 4c-e), Π_{14} in the SM solution is also enhanced at strong frontal features (Fig. S6c), which are again characterized by large magnitudes of cyclonic vorticity and convergence (Fig. S6d,e). Quantitatively however, the forward-flux magnitudes are generally weaker and shallower compared with the HF solution, in agreement with Fig. 3. There are some differences in the RMS and skewness values of ζ/f and δ/f between the HF and SM solutions, but these may just be a result of different numerical iterations of turbulent flows and are not necessarily associated with internal wave effects. Finally, the pattern correlation between regions of strong and positive Π_{14} values and regions of strong fronts is not as high as in the HF solution (Fig. 4a,b and Fig. S6a,b). This suggests that the IW-induced forward fluxes are especially concentrated at fronts, compared with the more traditional forward fluxes that are associated with submesoscale currents.

References

Argo. (2000). Argo float data and metadata from global data assembly centre (argo gdac). *SEANOE*.

Branellec, P., & Thierry, V. (2016). Rrex 2015. ctd-o2 data report. *ODE/LOPS/16-26*.

Branellec, P., & Thierry, V. (2018). Rrex 2017. ctd-o2 data report. *Rap. Int. LOPS/18-04*.

Carton, J. A., & Giese, B. S. (2008). A reanalysis of ocean climate using simple ocean data assimilation (soda). *Monthly weather review*, *136*(8), 2999–3017.

Dee, D., Balmaseda, M., Balsamo, G., Engelen, R., Simmons, A., & Thépaut, J.-N. (2014). Toward a consistent reanalysis of the climate system. *Bulletin of the American Meteorological Society*, *95*(8), 1235–1248.

Ducet, N., Le Traon, P.-Y., & Reverdin, G. (2000). Global high-resolution mapping of ocean circulation from topex/poseidon and ers-1 and-2. *Journal of Geophysical Research: Oceans*, *105*(C8), 19477–19498.

Egbert, G. D., Bennett, A. F., & Foreman, M. G. (1994). Topex/poseidon tides estimated using a global inverse model. *Journal of Geophysical Research: Oceans*, *99*(C12), 24821–24852.

Egbert, G. D., & Erofeeva, S. Y. (2002). Efficient inverse modeling of barotropic ocean tides. *Journal of Atmospheric and Oceanic technology*, *19*(2), 183–204.

Large, W. B. (2006). Surface fluxes for practitioners of global ocean data assimilation. In *Ocean weather forecasting* (pp. 229–270). Springer.

Large, W. G., McWilliams, J. C., & Doney, S. C. (1994). Oceanic vertical mixing: A review and a model with a nonlocal boundary layer parameterization. *Rev. of Geophys.*, *32*, 363–403.

Lemarié, F., Kurian, J., Shchepetkin, A. F., Molemaker, M. J., Colas, F., & McWilliams, J. C. (2012). Are there inescapable issues prohibiting the use of terrain-following coordinates in climate models? *Ocean Modelling*, *42*, 57–79.

Mason, E., Molemaker, J., Shchepetkin, A. F., Colas, F., McWilliams, J. C., & Sangrà, P. (2010). Procedures for offline grid nesting in regional ocean models. *Ocean Modelling*, *35*, 1–15.

Renault, L., Molemaker, M. J., McWilliams, J. C., Shchepetkin, A. F., Lemarié, F., Chelton, D., ... Hall, A. (2016). Modulation of wind work by oceanic current interaction with the atmosphere. *J. Phys. Oceanogr.*, *46*, 1685–1704.

Shchepetkin, A. F. (2015). An adaptive, courant-number-dependent implicit scheme for vertical advection in oceanic modeling. *Ocean Modelling*, *91*, 38–69.

Shchepetkin, A. F., & McWilliams, J. C. (2005). The Regional Oceanic Modeling System: A split-explicit, free-surface, topography-following-coordinate oceanic model. *Ocean Modelling*, *9*, 347–404.

Shchepetkin, A. F., & McWilliams, J. C. (2011). Accurate Boussinesq oceanic modeling with a practical, "stiffened" equation of state. *Ocean Modelling*, *38*, 41–70.

Vic, C., Ferron, B., Thierry, V., Mercier, H., & Lherminier, P. (2021). Tidal and near-inertial internal waves over the Reykjanes Ridge. *Journal of Physical Oceanography*, *51*(2), 419–437.

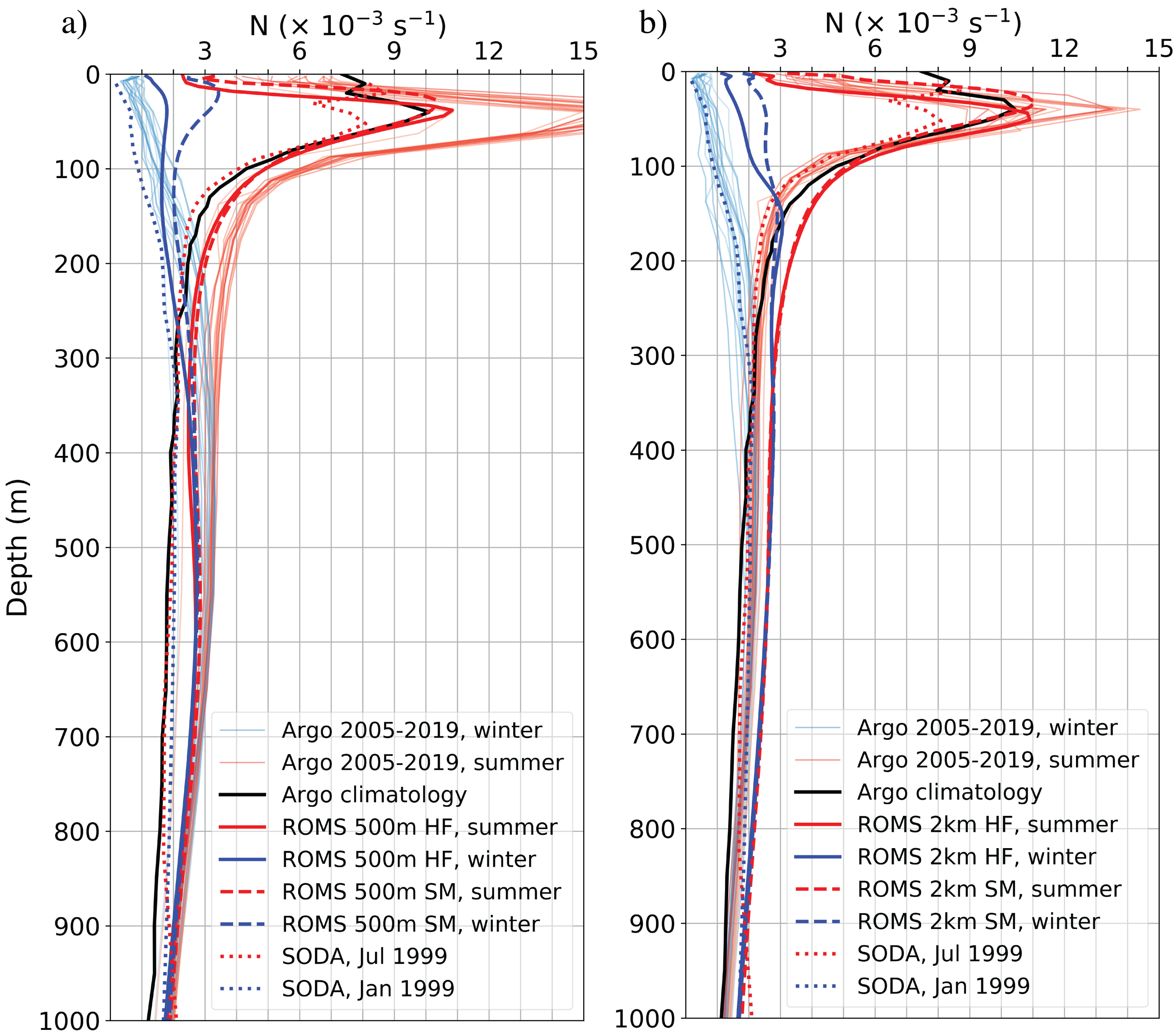

Figure S1: Same as Figure 1b for a) the 500 m solutions and b) the 2 km solutions.

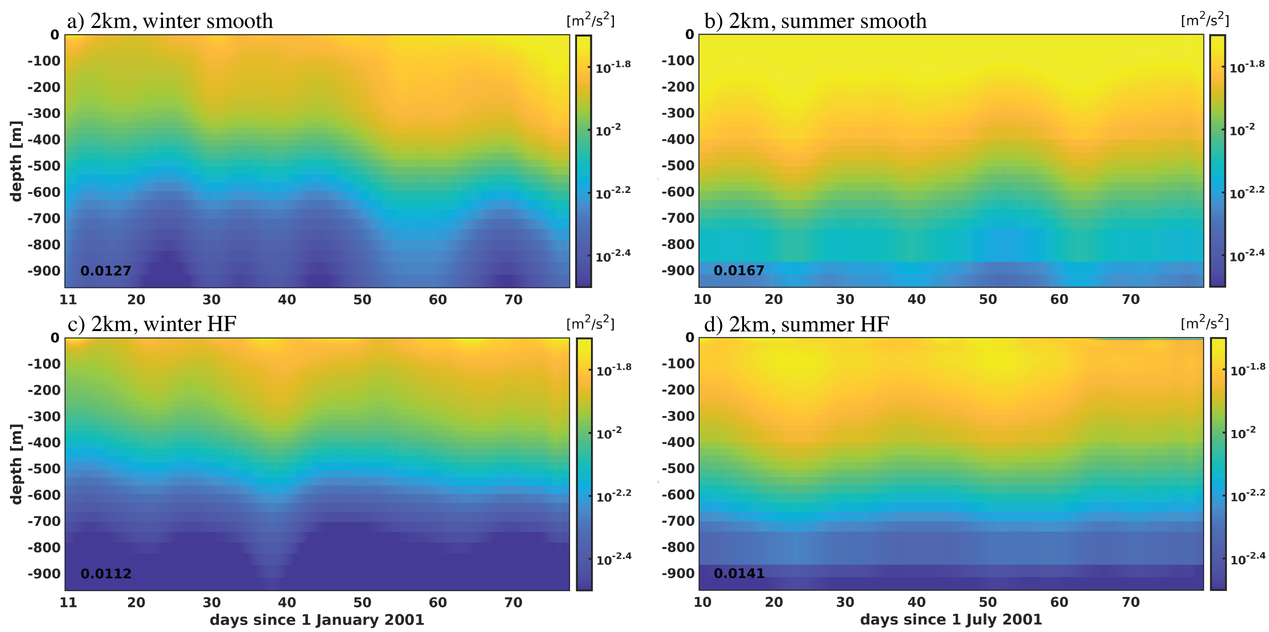

Figure S2: The horizontally-averaged low-passed KE in the 2 km solutions. HF denotes solutions with IW forcing and SM denotes solutions without IW forcing. Spatial averages are taken over the domain occupied by the 500 m grid (Fig. 1a). A sixth order Butterworth filter with a one week filter width is used for low-passing. The values in the lower left corner of each panel indicate the seasonal- and depth-averaged KE over the top 500 m.

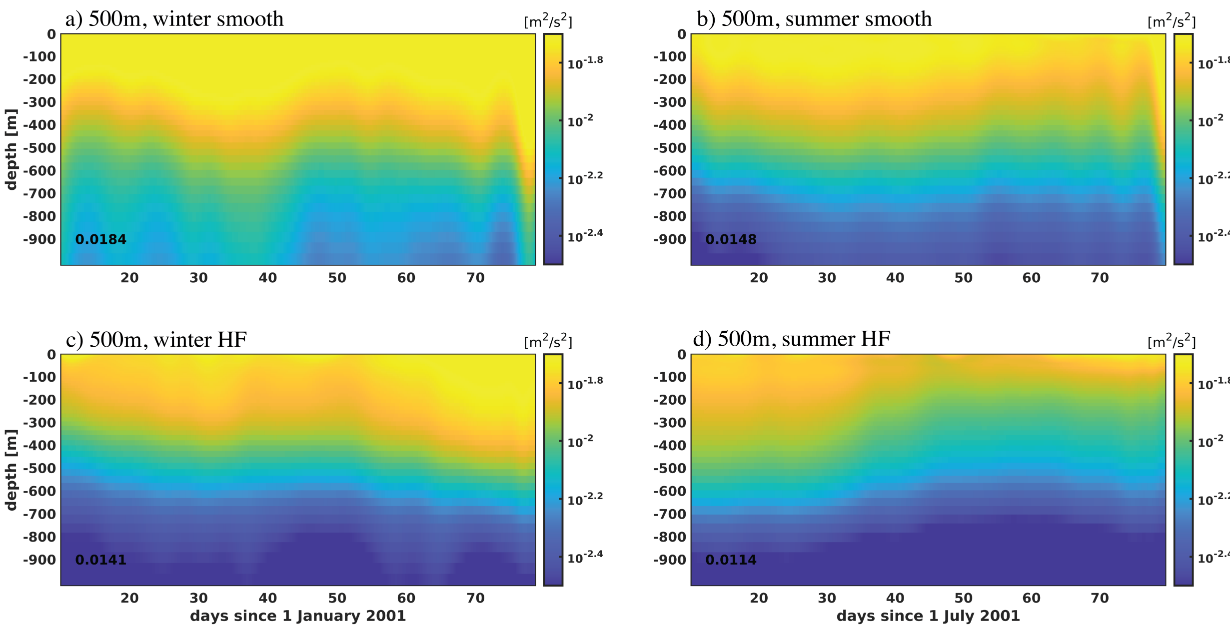

Figure S3: Same as Fig. S2 for the 500 m solutions.

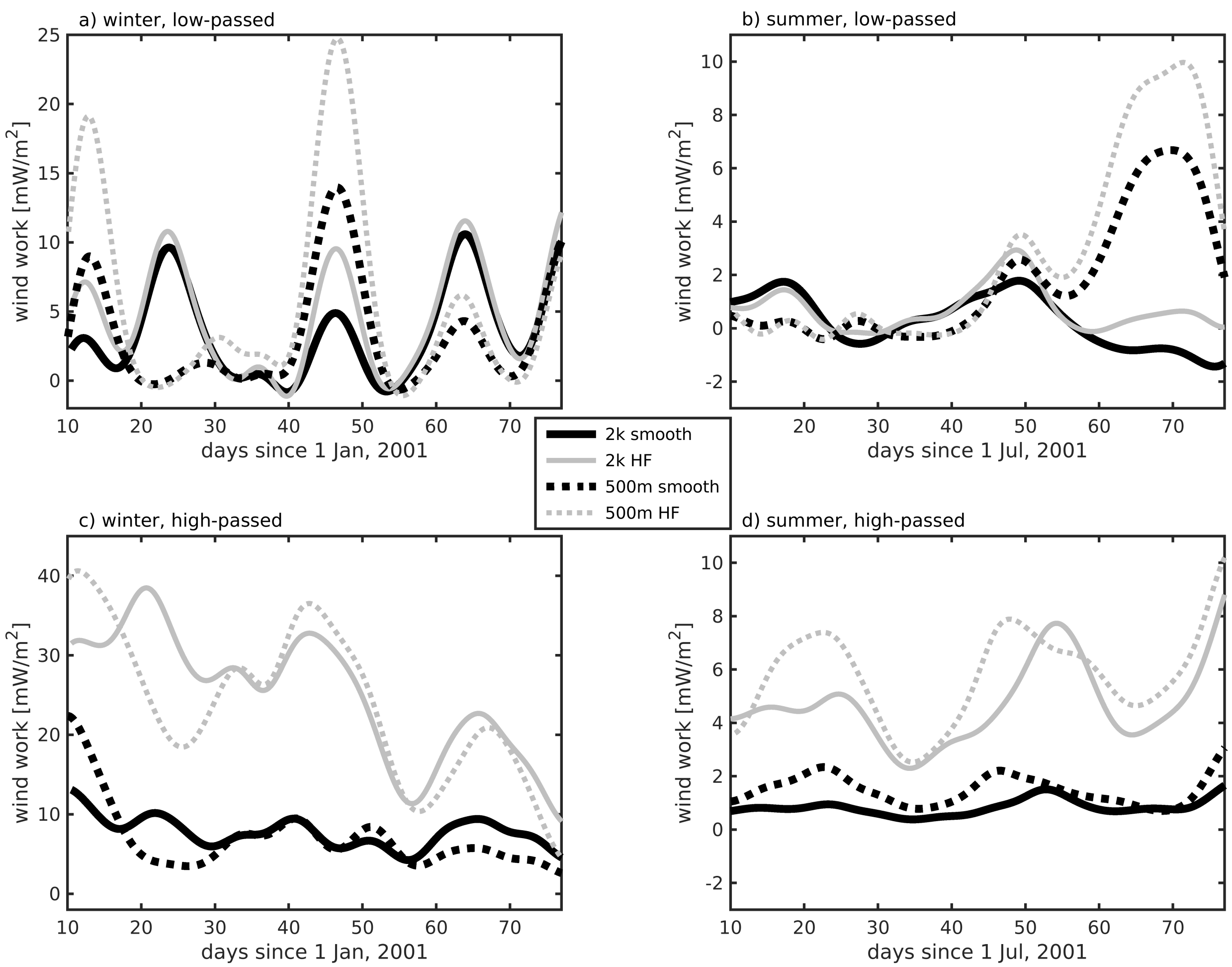

Figure S4: Seasonally- and horizontally-averaged a,b) low-passed and c,d) high-passed wind work for the solutions described in the text. Horizontal averages for the 2 km and 500 m solutions are computed over the domains shown in Fig. 1a. A sixth order Butterworth filter with a one week filter width is used for low-passing.

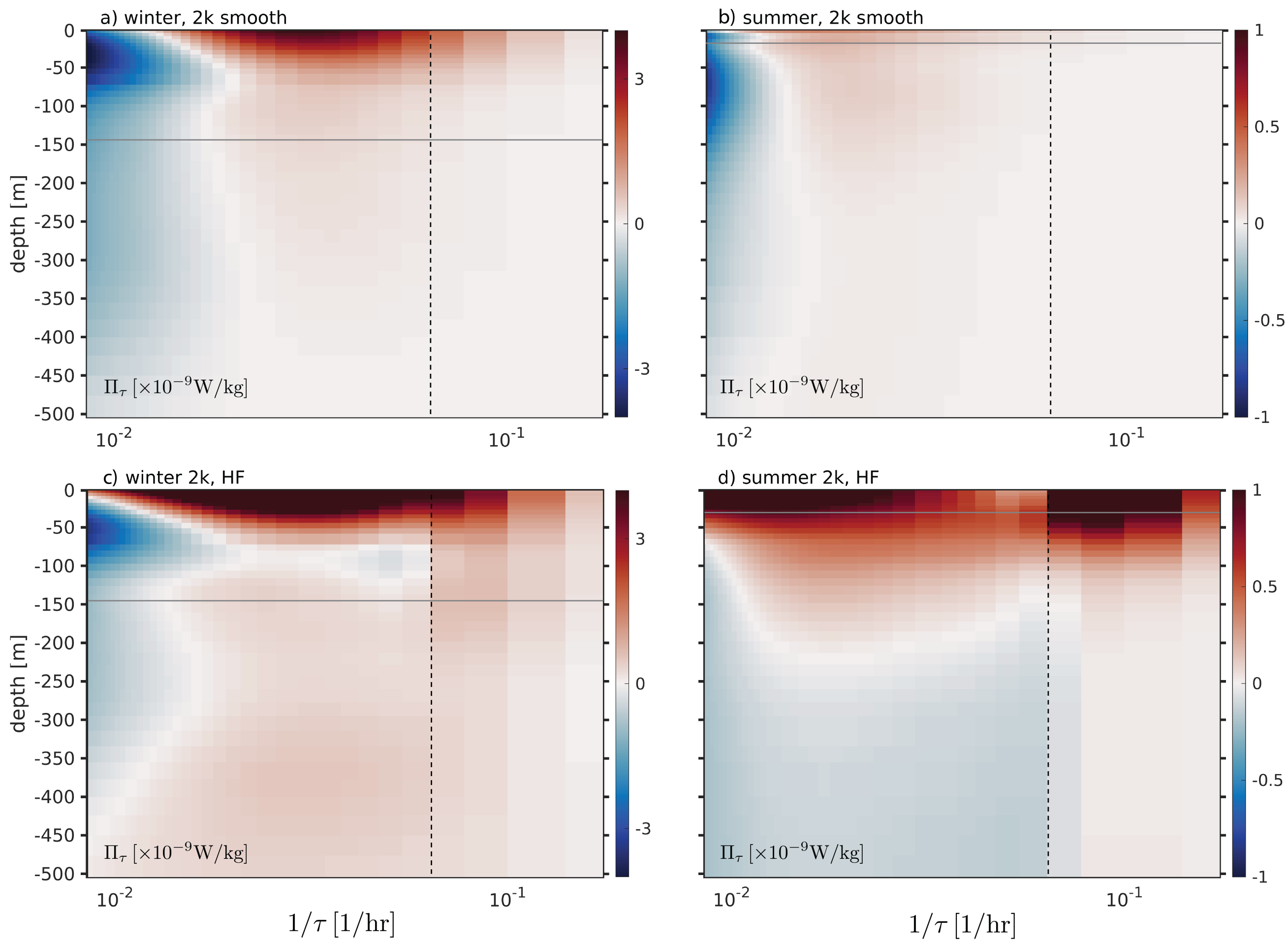

Figure S5: Same as Fig. 3 (panels c-f), but for the 2 km solutions. Horizontal averages are taken over the region occupied by the 500 m grid (Fig. 1a).

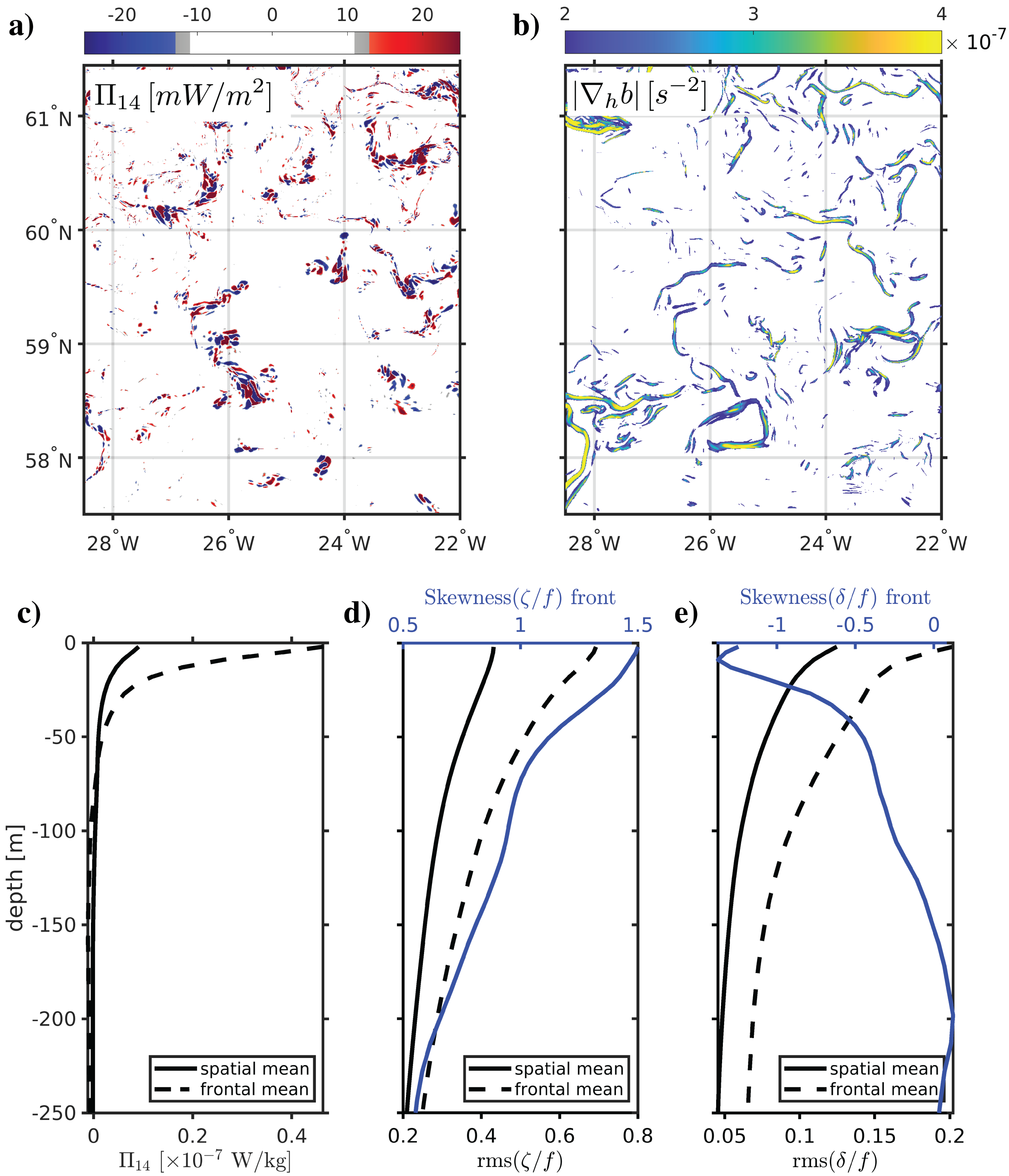

Figure S6: Same as Fig. 4, but for the 500 m smooth solution in winter.

Table S1: Seasonal- and depth-averaged low-passed KE in m^2/s^2 over the top 500 m, where a 6th order Butterworth filter with a 1 week filter width is used for low-passing. The averaging region (2 km grid or 500 m grid) are shown in Fig. 1a.

Grid resolution, averaging region	winter		summer	
	HF	SM	HF	SM
2km, 2km grid	0.0120	0.0156	0.0145	0.0233
2km, 500m grid	0.0112	0.0127	0.0141	0.0167
500m, 500m grid	0.0141	0.0184	0.0114	0.0148